metals

MDPI

Article

Characterization Study of an Oxide Film Layer Produced under CO_2/Steam Atmospheres on Two Different Maraging Steel Grades

Mauro Andres Cerra Florez [1,2,3,*], Gemma Fargas Ribas [2,3], Joan Josep Roa Rovira [2,3], Enrique Vilarrasa-Garcia [4], Enrique Rodríguez-Castellon [5], Ana Beatriz Ferreira Sousa [1], Jorge Luiz Cardoso [1] and Marcelo José Gomes da Silva [1]

1 LACAM-Department of Metallurgical and Materials Engineering, Campus do Picí, Universidade Federal do Ceará, Bloco 729, Fortaleza 60440-554, Brazil; biasousahp@gmail.com (A.B.F.S.); jorgeluizjlc@gmail.com (J.L.C.); mgsilva@ufc.br (M.J.G.d.S.)
2 Center for Structural Integrity, Reliability and Micromechanics of Materials (CIEFMA), Department of Materials Science and Engineering, Escola d'Enginyeria de Barcelona Est, Universitat Politècnica de Catalunya, 08019 Barcelona, Spain; gemma.fargas@upc.edu (G.F.R.); joan.josep.roa@upc.edu (J.J.R.R.)
3 Barcelona Research Center in Multiscale Science and Engineering, Escola d'Enginyeria de Barcelona Est, Universitat Politècnica de Catalunya, 08019 Barcelona, Spain
4 GPSA-Department of Chemical Engineering, Campus do Picí, Universidade Federal do Ceará, Bloco 1010, Fortaleza 60455-760, Brazil; e.vilarrasa.garcia@gmail.com
5 Department of Inorganic Chemistry, Crystallography and Mineralogy, Campus de Teatinos, University of Malaga, 29071 Málaga, Spain; castellon@uma.es
* Correspondence: mauro.cerra@gmail.com

Abstract: Currently, surface treatments lead to inducing a superficial layer of several nanometers up to micrometer, which in some cases can be protective. In this experimental work, an oxide layer was generated under different atmospheres (CO_2 and steam atmospheres) during the thermal aging treatment of two different maraging grades, 300 and 350. Afterwards, this layer was microstructural and mechanically characterized by advanced characterization techniques at the micro- and submicron length scale to highlight some information related to the generated oxide layer. The results showed that the oxide layer (in both grades) was made up of several compounds like: TiO_2, MoO_3, hematite (α-Fe_2O_3), and $CoFe_2O_4$, this being the majority compound distributed homogeneously throughout the layer. Furthermore, a nickel-rich austenitic phase at the interphase was mainly made up cobalt ions (Co^{2+}), instead of iron ions (Fe^{2+}), within the spinel lattice.

Keywords: maraging steel grades; oxide layer; microstructural characterization; sliding properties; spinel; nickel-rich austenitic phase

Citation: Florez, M.A.C.; Fargas Ribas, G.; Rovira, J.J.R.; Vilarrasa-Garcia, E.; Rodríguez-Castellon, E.; Sousa, A.B.F.; Cardoso, J.L.; Gomes da Silva, M.J. Characterization Study of an Oxide Film Layer Produced under CO_2/Steam Atmospheres on Two Different Maraging Steel Grades. *Metals* **2021**, *11*, 746. https://doi.org/10.3390/met11050746

Academic Editor: Francesca Borgioli

Received: 2 April 2021
Accepted: 28 April 2021
Published: 1 May 2021

1. Introduction

The oxidation process of maraging steels was addressed by several authors until the 1990s [1–5]. In each of these publications, different conditions such as time, atmosphere, and maraging steel grades were used to obtain an oxide layer with a spinel-type microstructure that could act as protective layer which is able to be employed in different sectors.

Klein et al. [1,2] observed that, during the oxidation process of steels under different atmospheres (CO_2, steam and air) at 485 °C for 3 h, it is possible to growth a spinel iron oxide Fe_3O_4, known as magnetite, as follows:

$$\text{Steam atmosphere: } 3Fe + 8H_2O = Fe_3O_4 + 4H_2O + 4H_2, \quad (1)$$

$$CO_2 \text{ atmosphere: } 3Fe + 4CO_2 = Fe_3O_4 + 4CO, \quad (2)$$

$$O_2 \text{ atmosphere: } 3Fe + 2O_2 = Fe_3O_4. \quad (3)$$

The common, growing oxide layer process for all these atmospheres may be associated to the diffusion process of iron ions from the metal to the oxide–gas interface, yielding as a result an oxide layer with one layer externally formed by magnetite and one near the interface with appreciable amounts of nickel and cobalt and poor amounts of iron and oxygen [1,2]. Furthermore, Klein et al. [3] investigated the oxide layer mechanisms of another maraging grade under a superheated steam atmosphere created because of the reaction diffusion process. They claimed that in the kinetic conditions, iron oxidizes faster than molybdenum, producing a magnetite (Fe_3O_4) layer that covers the formed MoO_3 and blocks its growth.

On the other hand, Rezek et al. [4] assessed the influence of the water vapor flow rate during the heat treatment of maraging 300 steel. They found that a higher flow rate forms an oxide composed practically of magnetite (with a maximum content of around 7% of hematite), while with a low flow rate, up to 40% of hematite is produced. Greyling et al. [5] studied the oxidation process for the same kind of maraging steel under an air atmosphere at different temperatures. In general, three different types of oxides were generated: a spinel, α-Fe_2O_3, and a mixture of CoO-α-Fe_2O_3, located in this order from the metal–oxide interface to the oxide–gas interface.

Within this context, scarce information related to the oxidation process of maraging steels grades is available in the literature. Within the aforementioned information, in this research, the microstructure and mechanical properties of the oxide layer process generated under different atmospheres (CO_2, water vapor, and nitrogen) for two different maraging steel grades (300 and 350) are investigated.

2. Materials and Methods

2.1. Materials

The two different kinds of maraging steels 300 (Mar300) and 350 (Mar350) (chemical composition for each is summarized in Table 1), were supplied by the Materials Characterization Laboratory (LACAM) of the Universidade Federal do Ceará (Ceará, Brazil). The specimens were cut using a metallographic saw to obtain samples with dimensions of $1 \times 1 \times 2$ cm^3, and subsequently annealed at 840 °C for 1 h. After the annealing process conducted at 840 °C for 1 h, the specimens were polished until reaching a mirror-like surface.

Table 1. Chemical composition of maraging steel grades (wt. %).

Samples	Fe	Ni	Co	Mo	Ti	Cr	V	Si	Al	C
Mar300	Bal.	18.28	9.51	4.80	0.73	0.12	0.10	0.08	0.07	<0.01
Mar350	Bal.	17.65	11.65	4.69	1.44	0.05	0.10	0.04	0.06	0.002

The thermal aging treatment was carried out in a tube oven with a gas inlet and outlet. Before the entrance of the oven, the line had three connections, one connected to a steam generator, and the other two connected to CO_2 and N_2 cylinders, respectively. The steam generator reached a temperature of 150 °C and it was necessary to use helium injection as a carrier gas to increase the flow rate. The experimental set-up used to create the oxide layer can be seen in Figure 1.

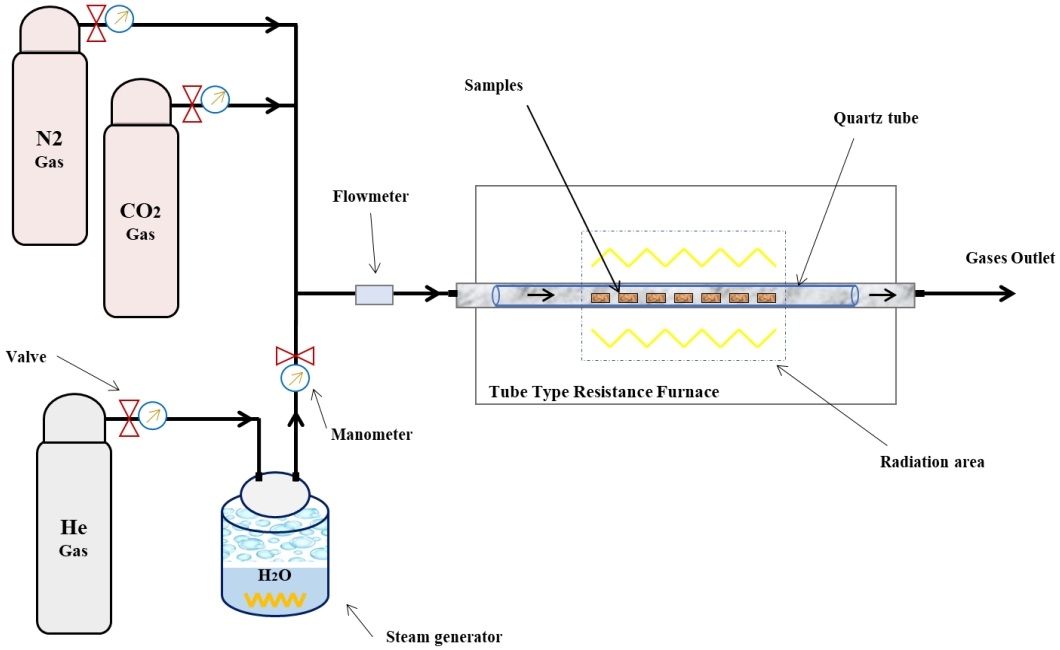

Figure 1. Experimental configuration of the devices for the aging heat treatment.

Each tested sample was placed inside the oven in a quartz tube and heated at 300 °C for 30 min under CO_2 atmosphere. Steam was added and the temperature was increased to 490 °C for 15 min. Shortly thereafter, the CO_2 gas was removed, and the temperature was kept constant and equal to 490 °C for 3 h only with steam and helium. The cooling process was performed with a constant N_2 flow during 3 h to avoid the generation of an overoxidation layer thickness.

2.2. Microstructurally Characterization

The phases present in both the steels as well as in the oxide layer were detected by X-ray diffraction (XRD) using the Philips X'Pert equipment (Co Kα radiation source) (Philips, Almelo, The Netherlands) with a wavelength (λ) of 1.789 nm and monochromator. The XRD measurements were conducted from $10° \leq 2\theta \leq 110°$, and the resolution was held constant and equal to 0.02°. The voltage and current were kept constant and equal to 40 kV and 45 mA, respectively, and the analysis of the patterns found was carried out in the X'PertHighScore Plus® software (version 4.9.0) from Panalytical®, Almelo, The Netherlands) and the semi-quantification (%) of the phases present in the oxide layer was done by using the reference intensity ratio (RIR) methodology [6,7].

The oxide layer formed on the samples was characterized by different advanced characterization techniques to better understand the different phases created during the oxidation process under different atmospheres. The confocal laser scanning microscope CLSM Carl ZEISS LSM 800 (Carl Zeiss, Oberkochen, Germany) and the White Light Interferometry (WLI) Optical interferometer Veeco Wyko 9300NT (Veeco Instruments, Plainview, NY, USA) were used to observe the oxide layer morphology. Furthermore, the main roughness parameters were measured to quantitatively assess the oxide layer topography by using the Wyko Vision® software (version 4.2, Veeco Instruments, Plainview, NY, USA), which includes: the arithmetic mean height (*Sa*), the maximum height (*Sz*), the maximum peak height (*Sp*), the maximum pit height (*Sv*) and the root-mean-square height (*Sq*). More information related to the roughness parameters are available in References [8–10].

The Phenom XL Desktop SEM microscope (ThermoFisher Scientific, Lenexa, KS, USA) with EDS detector was used to observe the oxide and obtain the chemical composition measurements. Furthermore, the oxide layer thickening as well as the microstructure was determined by focused ion beam (FIB) milling of cross-sections and scanning elec-

tron microscopy (SEM) inspection. It was done by using a dual beam workstation, field emission scanning electron microscopy (FE-SEM) Zeiss Neon 40 (Carl Zeiss NTS GmbH, Oberkochen, Germany).

To obtain the chemical composition of the oxide layer, three techniques were used, the Fourier transform infrared (FT-IR) spectroscopy was used on the Fourier Nicolet 6700 infrared spectrometer (Thermo Scientific, Lenexa, KS, USA), using the KBr pellet method at room temperature. RAMAN spectra were recorded on a Renishaw's inVia Qontor Raman microscope (Renishaw, Gloucestershire, UK) with a neon laser with $\lambda \sim 532$ nm, with an intensity analysis performed in Raman Environment (WiRE™) software (version 4.4, Renishaw, Gloucestershire, UK).

Finally, X-ray photoelectron spectroscopy (XPS) measurements were performed on the Physical Electronics spectrometer PHI Versa Probe II Scanning XPS Microprobe (Physical Electronics, Inc, Chanhassen, MN, USA) with monochromatic X-ray radiation Al Kα (1400 μm, 26.6 W, 5 kV, 1486.6 eV) and a double beam neutralizer. The experiments were carried out after cleaning the surface for two pickling cycles with argon (Ar^+) ions at 0.5 eV for 1 min and 1 keV for 5 min, respectively. XPS spectra were processed using the MultiPak 9.0 package (Physical Electronics, Inc, Chanhassen, MN, USA). The binding energy values were referenced to the C 1*s* adventitious signal at 284.8 eV, and the recorded spectra were fitted using Gauss–Lorentz curves. The atomic concentration percentages of the constituent elements on the surfaces of the samples were determined taking into account the sensitivity factor of the corresponding area for the different measured spectral regions.

2.3. Mechanical Properties: Scratch Tests

Nano-scratch tests were made with a nano-scratch attachment of the Nanoindenter XP (MTS) (Nanomechanics, Inc., Oak Ridge, TN, USA) that allows for lateral force measurements. A Berkovich indenter was used to scratch the surface under loading control mode. The load was linearly increased at a constant velocity of 10 μm/s for a total scratch length of 500 μm up to reaching 100 mN. Three different scratches were performed on each sample. The distance between scratches was held constant and equal to 500 μm to avoid any overlapping effect. The scratches marks were observed by using the field emission scanning electron microscopy (FE-SEM) Zeiss Neon 40 (Carl Zeiss NTS GmbH, Oberkochen, Germany).

3. Results

3.1. Steel Characterization

X-ray diffraction (XRD) diffractograms after the annealing treatment conducted at 840 °C for 1 h for both the maraging steel grades investigated here are depicted in Figure 2. The peaks {110}, {200}, and {211} correspond to the martensitic (α'-) phase in fair agreement with preliminary works [11,12].

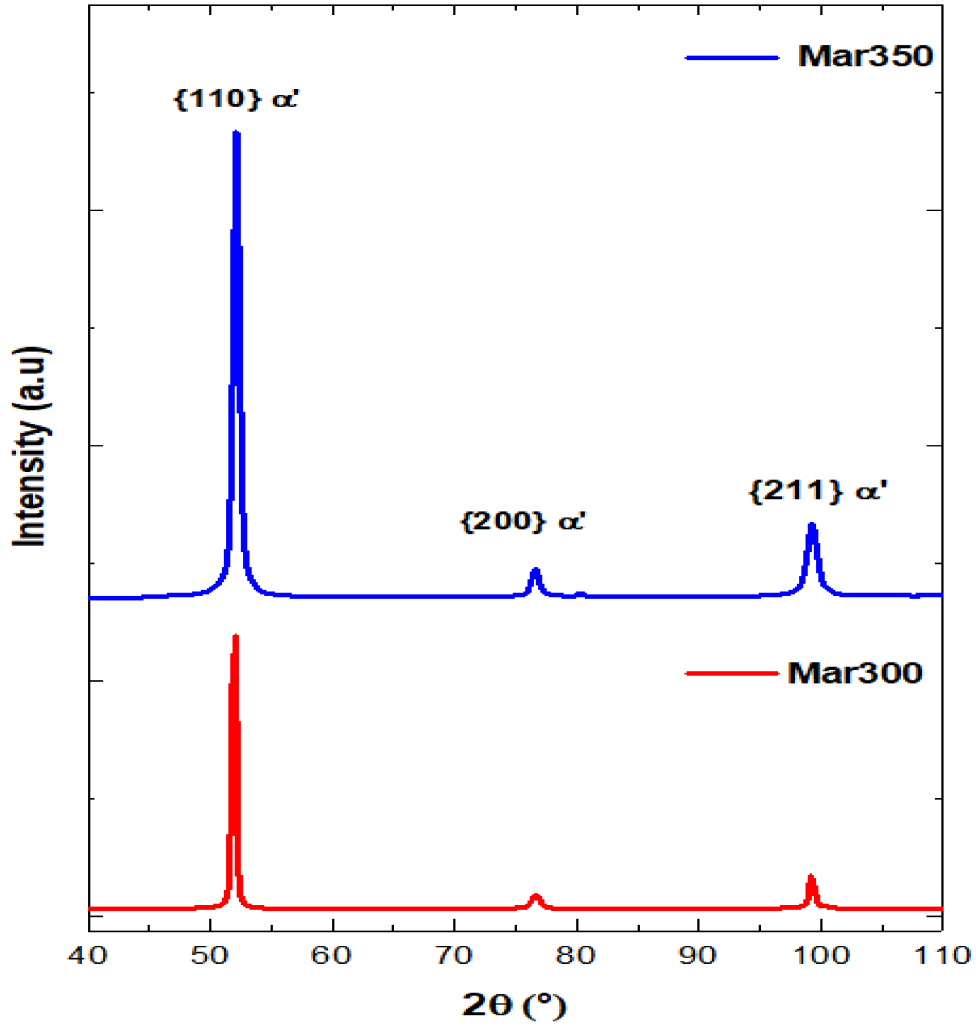

Figure 2. X-ray diffraction (XRD) diffractograms for the thermally treated specimens for both maraging steel grades.

3.2. Oxide Characterization

The oxide layer for both samples was observed by confocal laser scanning microscope (CLSM) covering the entire surface. Both maraging steel grades presented several heterogeneities distributed along the created oxide layer, such as ridges, valleys, cracks, and peeling, as shown in Figure 3. The different defects present in the oxide layer may be related to the expansion coefficient between the phases heterogeneously distributed along the entire oxide layer. Additionally, the present defects could be related with the presence of water molecules condensed on the surface of the oxide layer, which starts to degrade the oxide layer.

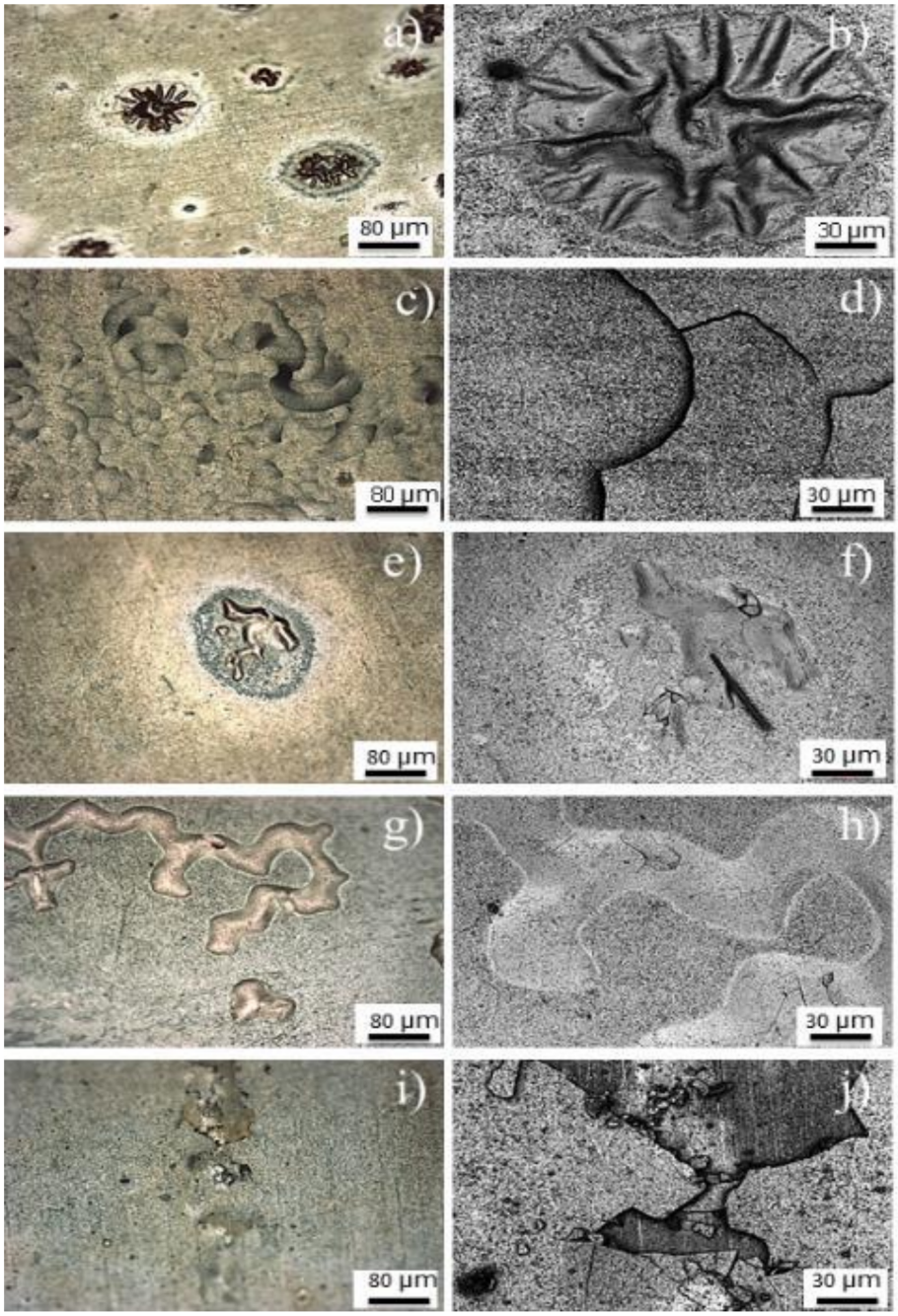

Figure 3. Optical (**a**,**c**,**e**,**g**,**i**) and confocal laser scanning microscope (CLSM) (**b**,**d**,**f**,**h**,**j**) micrographs of the heterogeneities found on the oxide layer for each maraging steel grade investigated here.

The roughness profile for each oxide layer was investigated by optical interferometry, and the 3D topography profiles are shown in Figure 4. From this image it is possible to determine the main roughness parameters, such as arithmetic mean height (*Sa*) and maximum height (*Sz*), as well as other parameters that are described and summarized in Table 2. From this observation, it is possible to conclude that the oxide layer does not grow homogeneously due to the presence of several nodules.

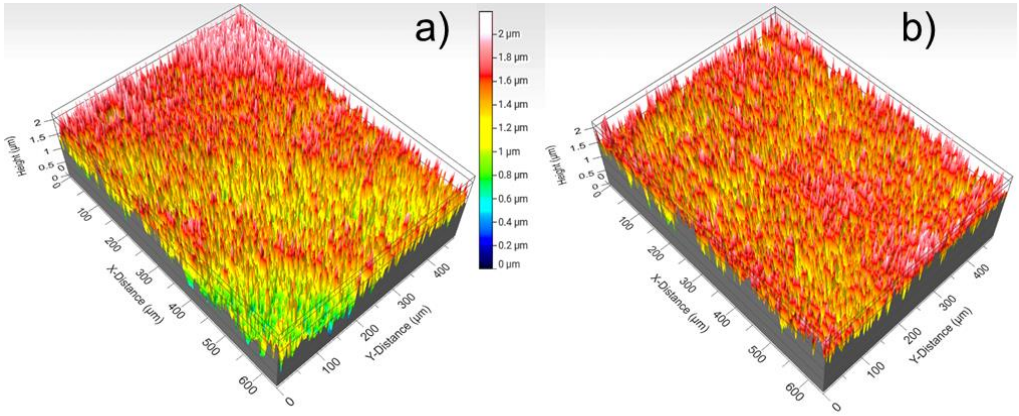

Figure 4. Interferometry 3D topography of the oxide surface produced on (**a**) Mar300 and (**b**) Mar350 maraging steels.

Table 2. The main 3D roughness parameters according to ISO 25178.

Roughness Parameter	Oxide of the Mar300 (µm)	Oxide of the Mar350 (µm)
Arithmetic Mean Height (*Sa*)	0.21	0.20
Maximum Height (*Sz*)	2.22	2.19
Maximum Peak Height (*Sp*)	0.90	0.85
Maximum Pit Height (*Sv*)	1.32	1.34
Root-Mean-Square Height (*Sq*)	0.31	0.25

The oxide layer morphology from each condition and maraging steel grade was observed by scanning electron microscopy (SEM) and is depicted in Figure 5. Figure 5a shows that it is possible to observe a completely covered surface without any superficial defect, and with several heterogeneities, including valleys and cracks (see white circles). On the other hand, in Figure 5b, nodular formations with different layers, sizes, and porosities are observed in more detail. The points highlighted with the letters A and B identify the positions where the chemical analysis by energy dispersive X-ray (EDS) was performed, and are summarized in Table 3, which highlights the chemical composition variation. From this observation, it is possible to observe that the metal base is richer in iron, nickel, titanium, and molybdenum, while the upper part of these nodules is mainly rich in cobalt.

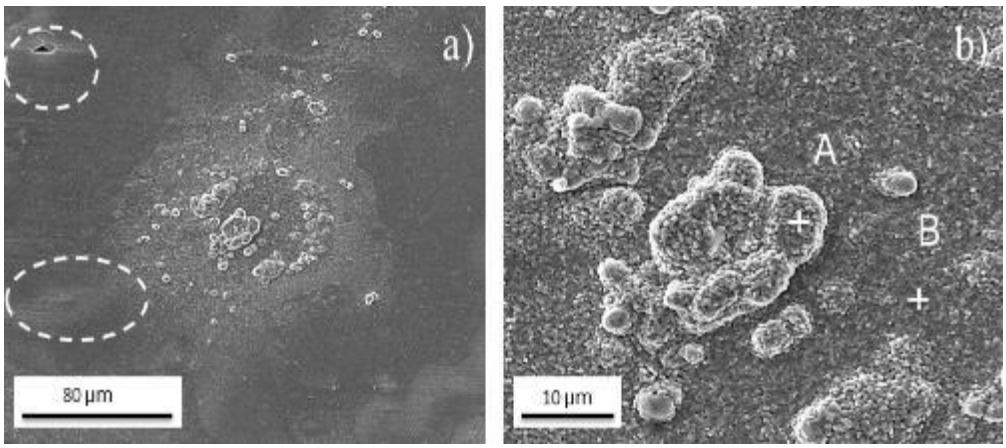

Figure 5. Scanning electron microscopy (SEM) micrographs of the oxide formed on Mar300 maraging steel, (**a**) different heterogeneities found on the surface of the oxide and (**b**) magnification of the nodular formation on the oxide.

Table 3. Energy dispersive X-ray (EDS) spot measurements taken at the different locations shown in the scanning electron microscopy (SEM) micrograph in Figure 5b.

EDS Quantitative Analysis from A and B Points (Weight Conc.)			
Element Number	**Element Symbol**	**Point A**	**Point B**
26	Fe	52.57	60.25
8	O	32.46	27.70
27	Co	13.64	9.47
28	Ni	0.69	1.48
42	Mo	0.59	0.95
22	Ti	0.05	0.15

In Figure 6a, it is possible to observe different heterogeneities dispersed in the different oxide layers for both maraging steel grades, which are identified with white circles, including cracks, ridges, valleys showing the internal oxide, and areas with different straight edges presenting the limits of the chemical composition. On the other hand, Figure 6b shows a high-magnification SEM micrograph of the main defects. Furthermore, in this image, punctual EDS analysis was also carried out on each defect and the results are summarized in Table 4. As is depicted in this table, there was a difference between points A (located at the homogeneous surface oxide layer) and B (surface valley). The main difference between each point may be associated with the generation of different phases along the oxide layer. On the other hand, point C, located in a nodule at the top of the ridges, presented a composition close to point A, which suggests that the latter is formed above the ridges. At point D, which corresponds to the internal part of the oxide layer, a higher concentration of the main steel elements can be seen. This information confirms a difference in concentration for the different oxide layers. These differences from a chemical and morphological point of view may indicate the existence of different phases or compounds dispersed along the oxide layer thickness. Finally, the EDS spectra conducted inside a rectangular pore shape (point E) with straight edges presented a chemical composition rich in titanium and nitrogen, which may be related to the formation of titanium nitride (TiN) generated during the solidification process in concordance with results previously reported by Capurro et al. [13] and Silva et al. [14].

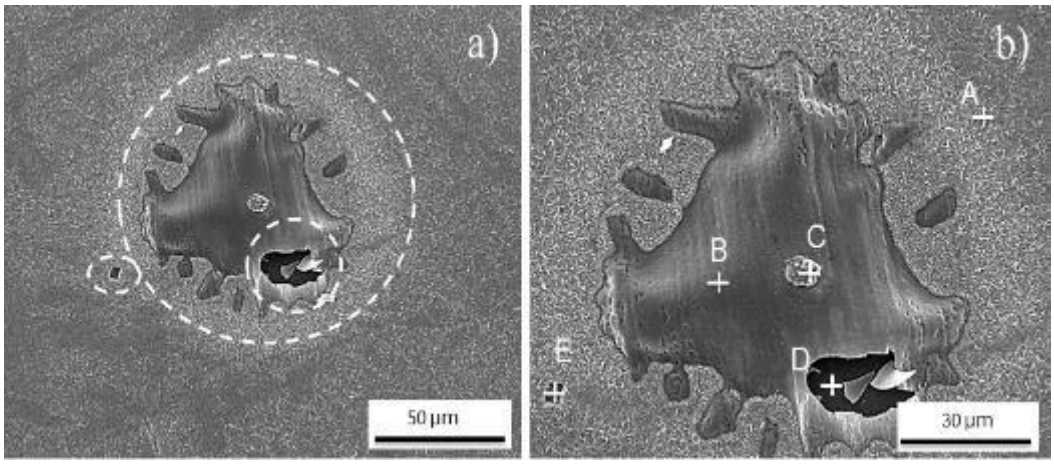

Figure 6. Scanning electron microscopy (SEM) micrographs of the oxide formed on Mar300 maraging steel, (**a**) different heterogeneities found on the surface of the oxide and (**b**) magnification of the defects found on the oxide.

Table 4. Energy dispersive X-ray (EDS) spot measurements taken at the different locations shown in the Scanning electron microscopy (SEM) micrograph in Figure 6b.

EDS Quantitative Analysis at Points A and B (Weight Conc.)						
Element Number	**Element Symbol**	**Point A**	**Point B**	**Point C**	**Point D**	**Point E**
26	Fe	62.65	60.22	62.50	60.98	3.92
8	O	32.68	38.10	32.34	19.11	31.43
27	Co	3.21	0.64	3.39	9.14	0.63
28	Ni	0.35	0.53	0.90	4.90	-
42	Mo	0.94	0.29	0.71	4.66	-
22	Ti	0.17	0.22	0.16	1.21	44.54
7	N	-	-	-	-	19.48

A detailed inspection of the broken oxide fragments and internal oxide layer is shown in Figure 7a. Linear EDS analysis was performed on the white dash line drawn in Figure 7a to compare the internal and external zone of the oxide layer from a chemical point of view (Figure 7b). As is shown, different chemical elements were present in both areas, confirming that the outer part was richer in iron than the inner one.

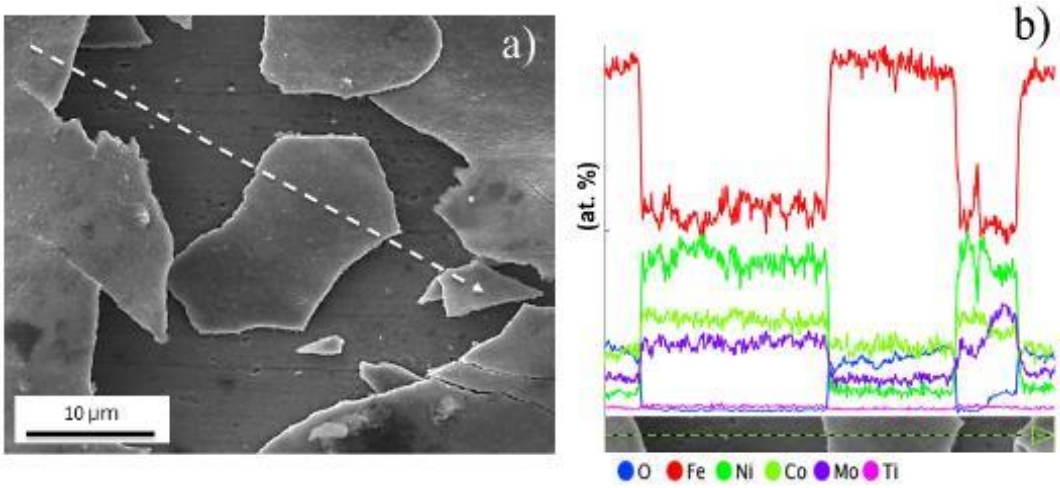

Figure 7. (**a**) Scanning electron microscopy (SEM) micrograph and (**b**) linear energy dispersive X-ray (EDS) spectrum made on the white dash line of the Figure 7a of the oxide surface formed on Mar300 maraging steel.

The heterogeneities observed for the Mar300 maraging steel also were found in the oxide layer in the Mar350 maraging steel. It is necessary to highlight that some imperfections reported previously for the Mar300 maraging steel (see Figure 6) did not exist in the oxides of Mar350 maraging steel, as depicted in Figure 8a, where, in the oxide region, several protuberances and broken areas are clearly visible. Figure 8b shows a magnification of the broken oxide area and the exposed internal oxide. EDS measurements were performed at the indicated points (A: protuberance on the oxide, B: internal part of the oxide, and C: more homogeneous part of the oxide) and the measurements are summarized in Table 5. These results show that the cobalt concentration was close between the internal region and that of the homogeneous oxide layer. Furthermore, the oxide layer presented an increase in the amount of molybdenum and nickel compared to the same area of the oxide formed in the Mar300 maraging steel (see values reported for the point A in Table 4). This difference between both grades may be related to the higher content of cobalt in the chemical composition of steel, which helps the formation of precipitate phases rich in molybdenum during the aging thermal treatment.

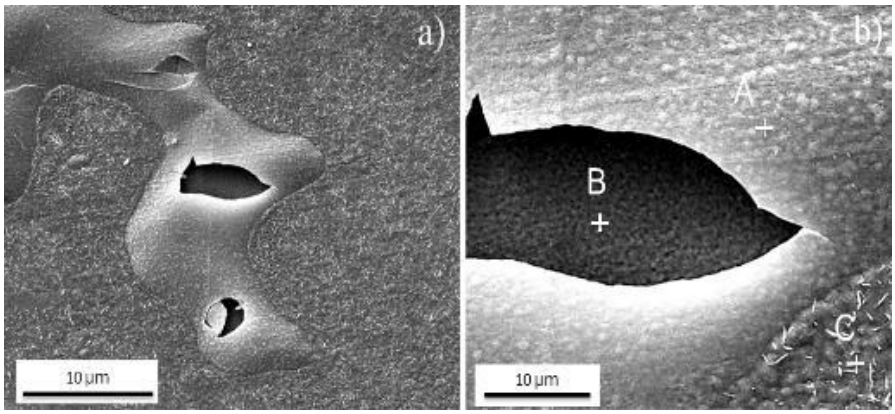

Figure 8. Scanning electron microscopy (SEM) micrographs of the oxide formed on Mar350 maraging steel: (**a**) different heterogeneities found on the surface of the oxide and (**b**) magnification of a broken area of the oxide (A: protuberance on the oxide, B: internal part of the oxide, and C: more homogeneous part of the oxide).

Table 5. Energy dispersive X-ray (EDS) spot measurements taken at the different locations shown in the scanning electron microscopy (SEM) micrograph in Figure 8b.

EDS Quantitative Analysis from Points A and B (Weight Conc.)				
Elem. Number	**Elem. Symbol**	**Point A**	**Point B**	**Point C**
26	Fe	62.61	55.23	59.43
8	O	34.84	27.97	34.01
27	Co	1.25	4.41	4.24
28	Ni	0.67	5.23	0.79
42	Mo	0.42	5.19	1.30
22	Ti	0.21	1.98	0.23

Other defects that were heterogeneously distributed along the oxide layer for both grades were the protuberances, as shown in Figure 9a,c. The images suggest that these protuberances were formed by different phases. A high magnification of these defects is shown in Figure 9b,d, and the interphase between this defect and the oxide layer is delimited by white dotted lines.

To observe the microstructure and to determine the oxide layer thickness, a cross-section using the focused ion beam (FIB) technique was used. Figure 10 presents the field emission scanning electron microscopy (FE-SEM) micrographs done on the oxide layer growth on Mar300 (Figure 10a,c) and Mar350 (Figure 10b,d) maraging steels. In both films, it is possible to observe the presence of little micro-holes, and mainly, a blister-like part of the film; this last defect present in the oxide layer (mentioned previously as protuberances) is related to differences in the expansion coefficient between the different constitutive phases, as well as being related to chemical heterogeneities along the oxide layer. From Figure 10c (oxide produced on Mar300) it was possible to observe that the oxide was not both homogeneous and continuous. In this sense, there is an air bubble that divides the oxide into two parts. The part of the oxide located above the bubble was the one with the thickest layer with a value ranging between 825 and 1310 nm; however, it was not homogeneous. From this SEM micrograph, it was also possible to distinguish two different kinds of oxide layers, one more obscure (external) and one clear (internal), which may be related to the presence of two different phases or compounds. The part of the oxide below the gas bubble was more homogeneous and its thickness ranged between 601 to 790 nm. It was also possible to observe a small microstructure of fine grains with a different shade just below the oxide. From Figure 10e (oxide produced on Mar350) it is possible to observe an homogeneous oxide layer with a thickness of approximately 1700 nm; however, another part of the oxide was also appreciated with a gas bubble that divided the oxide in two

different parts and which produced small cracks on their vertex. The part of the oxide located above it was small and relatively homogeneous, with a homogeneous thickness that ranged between 624 and 652 nm. Furthermore, differences in shades that may be attributed to the presence of two different phases and/or compounds were also observed. The part of the oxide below the gas bubble ranged between 865 and 1040 nm of thickness. In the same way as in Figure 10c, it is possible to observe the small fine-grained microstructure with a different shade just below the oxide. The lighter area on the outermost part of the oxide is due to the formation of more oxidized compounds, and the small metallic microstructure just below the metal–oxide interface with an austenitic-rich phase in Ni and Co formed because of the oxidation process [1–5].

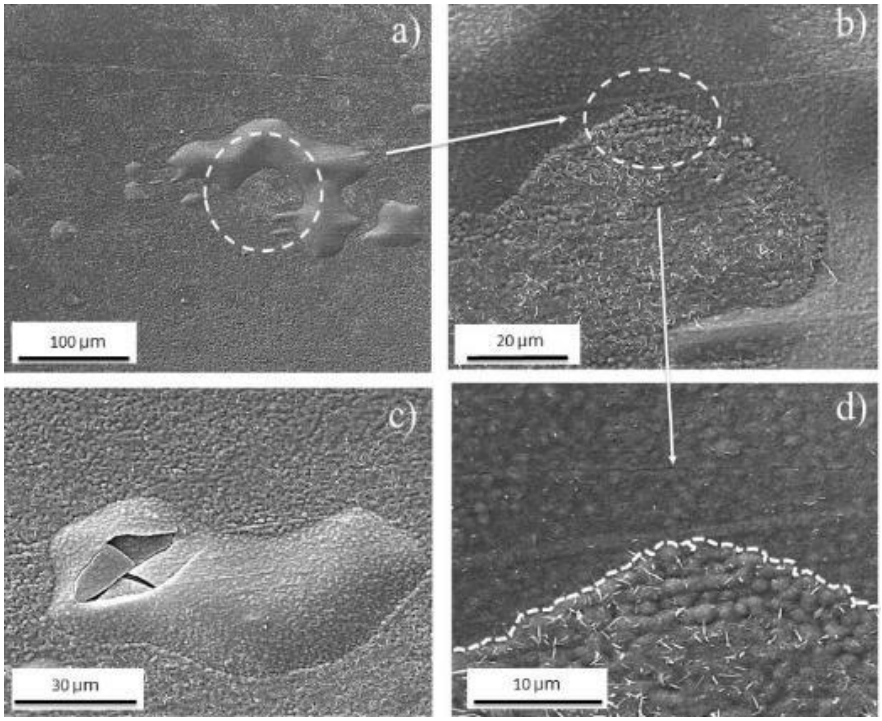

Figure 9. Scanning electron microscopy (SEM) micrographs of the oxide formed on Mar350 maraging steel: (**a**,**c**) different heterogeneities found on the surface of the oxide and (**b**,**d**) magnification of the protuberances found on the oxide.

The results of the X-ray diffraction (XRD) analysis of the oxide layers for both steels are shown in Figure 11. In the two oxides, the same phases labeled as A, B, C, D, and E were identified, where the A peaks corresponded to a spinel ferrite, which may be iron, cobalt, nickel, or a mixture of them, according to References [15,16]. On the other hand, it was not possible to determine which types of spinel were formed because they have the same crystallographic structure and lattice parameters [1]. The B peaks corresponded to hematite (Fe_2O_3) in agreement with Reference [15]. The peaks labeled with C corresponded to TiO_2 [15], while the D peaks corresponded to molybdenum oxide (MoO_3) [15,17]. Finally, the E peak corresponded to the austenite phase [12]. This phase was rich in Ni, Fe, and Co [1–4] and formed at the metal–oxide interface during the oxidation process when iron, cobalt, molybdenum, and titanium were oxidized and diffused through the oxide layer, leaving the steel surface with a high concentration of nickel; this phase is the microstructure of fine-grained metal with a darker color just below the oxide observed in Figure 10c,d.

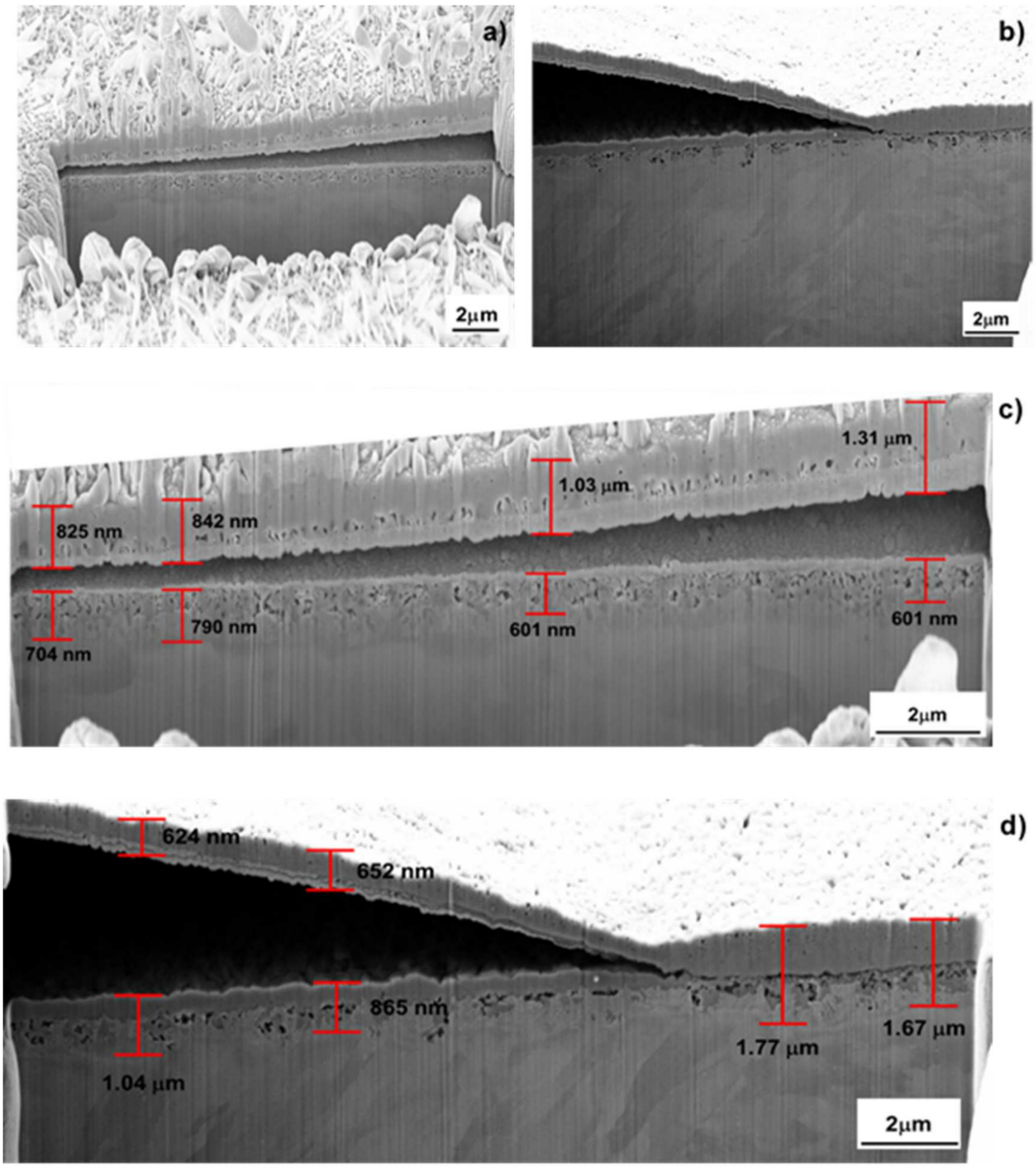

Figure 10. Field emission scanning electron microscopy (FE-SEM) cross-section micrograph and the magnification with the oxide layer thickness measurement on maraging 300 (**a**,**c**) and 350 (**b**,**d**) steels.

The semi-quantification of the phases presents in the oxides led to the determination of the phase formed in the oxide layer. The oxide layer created for the Mar300 maraging steel was mainly constituted by about 69.3% spinel, 23.8% hematite, 5.9% MoO_3, and 1% TiO_2. On the other hand, the other oxide layer was constituted by about 65% spinel, 23% hematite, 10% MoO_3, and 2% TiO_2. It is understandable that a higher amount of titanium oxide was found in Mar350 maraging steel due to the higher amount of this element in the chemical composition of this steel; however, the increase in the amount of molybdenum oxide cannot be associated with the amount of molybdenum in the chemical composition of this steel. The molybdenum content was almost identical in both steels, and this increase could thus be due to the greater amount of cobalt that was used to decrease the solubility of molybdenum in steel, which produces a greater amount of intermetallic precipitates rich in molybdenum and titanium during the aging heat treatment [18–21]; therefore, it is possible that on the surface of the maraging steel, this phenomenon provided a greater quantity of these elements that reacted and formed these oxides.

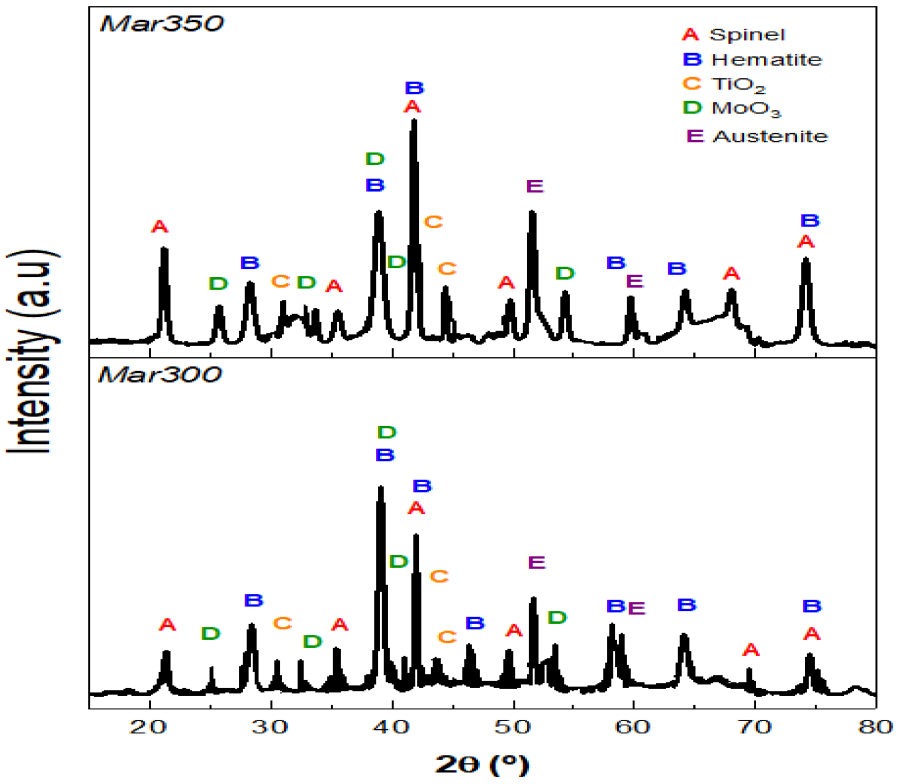

Figure 11. X-ray diffractograms of the oxide layer produced on the investigated maraging steels.

The Fourier transform infrared (FT-IR) spectra collected for the oxides of both steels are shown in Figure 12. The band located at 640 cm^{-1} corresponded to the of stretching vibration of Fe-O bonds in the structure of α-Fe_2O_3 (hematite), in agreement with Reference [22]. On the other hand, the band located at 586 cm^{-1} corresponded to the stretching vibration of the Fe-O links in tetrahedral locations of the cobalt spinel structure—$CoFe_2O_4$—as reported previously [23–26]. Likewise, there were characteristic bands of MoO_3 at 993 cm^{-1} due to vibrations in the Mo=O bonds within the molecule, and at 859 cm^{-1} due to Mo-O-Mo bonds that connect the different molecules [27,28].

Figure 13 shows the Raman spectra for the oxide layer of each maraging steel grade investigated here. However, in both oxide layers, the same species were found. Hematite (α-Fe_2O_3) labeled as A [29,30], spinel cobalt ferrite $CoFe_2O_4$ bands (B) [24,31,32], and Molybdenum oxide (MoO_3) were identified (C) [17,33,34]. As was clearly evident in the FT-IR and RAMAN spectra, it was not possible to detect the titanium oxides, and this is an indication that this element was in the innermost layers.

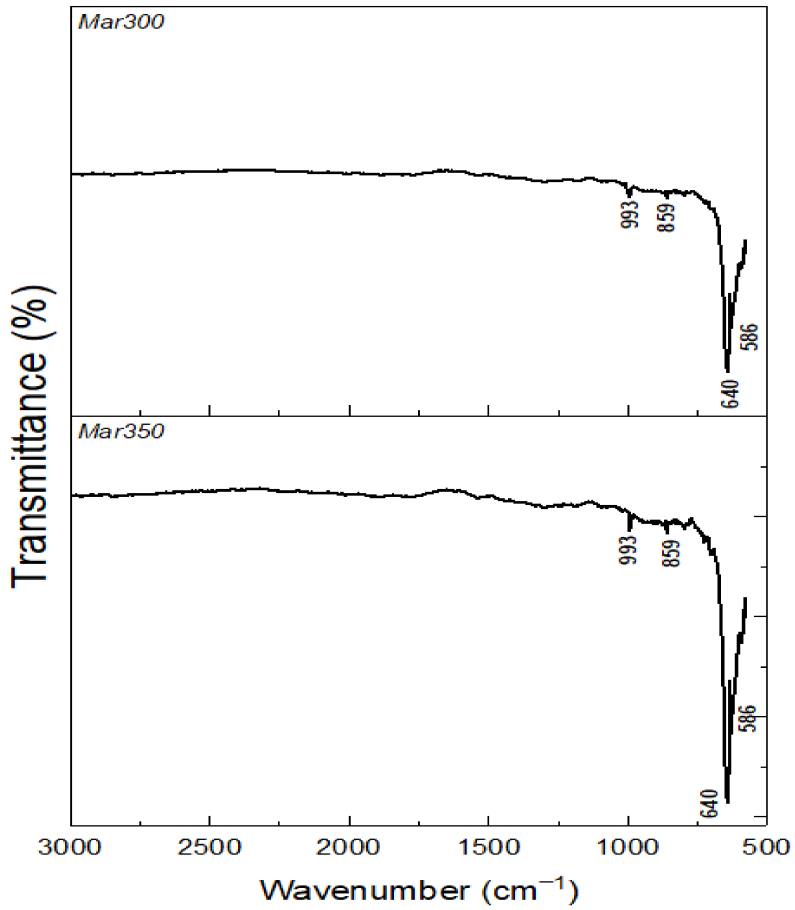

Figure 12. Fourier transform infrared (FT-IR) spectra of oxides produced on the maraging steels investigated here.

Figure 14a shows the survey X-ray photoelectron spectroscopy (XPS) spectrum of the oxide produced in Mar300 maraging steel, where the signals of the elements iron (Fe 2*p* and Fe 3*p*), carbon (C 1*s*), cobalt (Co 2*p*), and oxygen (O 1*s*) stand out. The chemical composition (in atomic concentration %) is also identified. Figure 14 also shows the high-resolution C 1*s* (b), O 1*s* (c), and Fe 2*p* (d) core-level spectra of the oxide produced on the maraging steel 300 grade before and after sputtering for 5 min with Ar^+ plasma. Tables 6 and 7 include the binding energy values (in eV) of the studied signals and the surface chemical composition, respectively. The C 1*s* core-level spectrum could be decomposed into four contributions (see Table 6). The main contribution at 284.8 eV was assigned to adventitious carbon, the other minor contributions at 285.6, 286.4, and 288.1 eV were derived from the presence of C-O, C=O, and O=C-O bonds, respectively [35,36]. After etching for 5 min, there were only two contributions at 284.8 and 286.0 eV, and the surface concentration of C decreased from 47.94% to 18.4% (see Table 7), being indicative, as expected, of a adventitious contamination, which is very common on the surface of metals. The assignment of the oxygen species in the O 1*s* signal was not easy. The O 1*s* signal can be decomposed into three contributions at 529.3, 531.2, and 532.4 eV. The contribution at 529.3 eV, denoted as Oα, can be related to the presence of surface lattice oxygen (O^{2-}), whereas the contribution at 531.2 eV, denoted as Oβ, was assigned to the presence of defect oxide or to the surface low coordination oxygen ion. The third contribution at 532.4 eV mainly proceeded from the hydroxyl groups and C-O and C=O groups. After etching for 5 min, the relative intensity of the contribution due to lattice oxygens increased, and the relative intensity of the other two contributions decreased because of the removal of the surface contamination. In fact, the oxygen surface content slightly increased after etching, from 38.57% to 42.34% (see Table 7) [37,38].

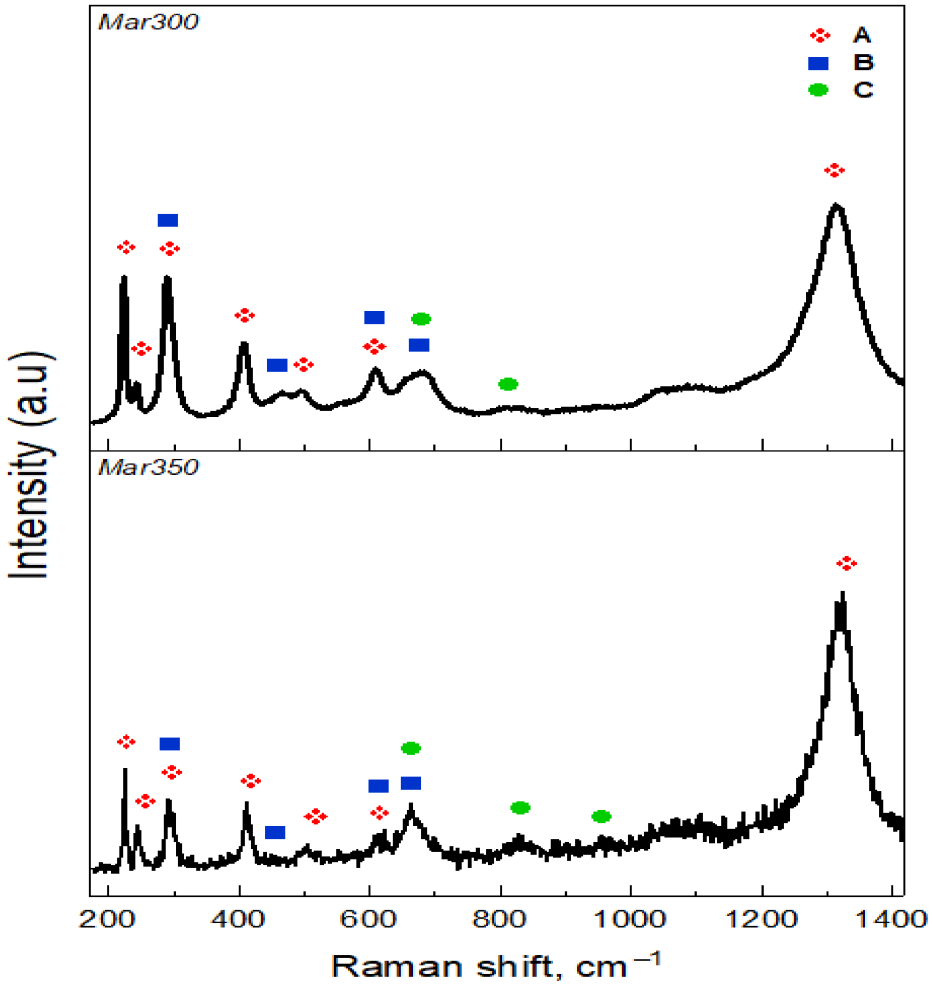

Figure 13. Raman spectra of oxides produced for the maraging steels investigated here.

Table 6. Binding energy values (in eV) of the studied elements, the percentages of the relative area in brackets, and the $Fe^{2+}/(Fe^{2+} + Fe^{3+})$ ratios for the studied oxide produced on maraging steels before and after etching for 5 min with Ar^+ plasma.

Sample	C 1*s*	O 1*s*	Fe $2p_{3/2}$	Co $2p_{3/2}$	Mo $3d_{5/2}$	$Fe^{2+}/(Fe^{2+} + Fe^{3+})$
Mar300	284.8 (82) 285.6 (8) 286.4 (5) 288.1 (5)	529.3 (63) 531.2 (24) 533.4 (13)	709.2 (43) 710.8 (48) 712.9 (9)	781.3	232.1	43
Mar300 5 min Ar^+	284.8 (95) 286.0 (5)	529.7 (78) 531.2 (14) 532.2 (8)	708.9 (50) 710.5 (37) 712.6 (13)	780.7 782.0		53
Mar350	284.8 (80) 286.0 (13) 288.0 (7)	529.7 (72) 531.2 (16) 532.4 (12)	708.5 (17) 710.2 (60) 712.4 (23)	780.7 782.7	232 (59) 232.7 (41)	17
Ma350 5 min Ar^+	284.8 (96) 287.4 (4)	529.8 (78) 531.1 (15) 532.4 (7)	708.4 (40) 710.0 (35) 712.4 (25)	782.3	232.1	40

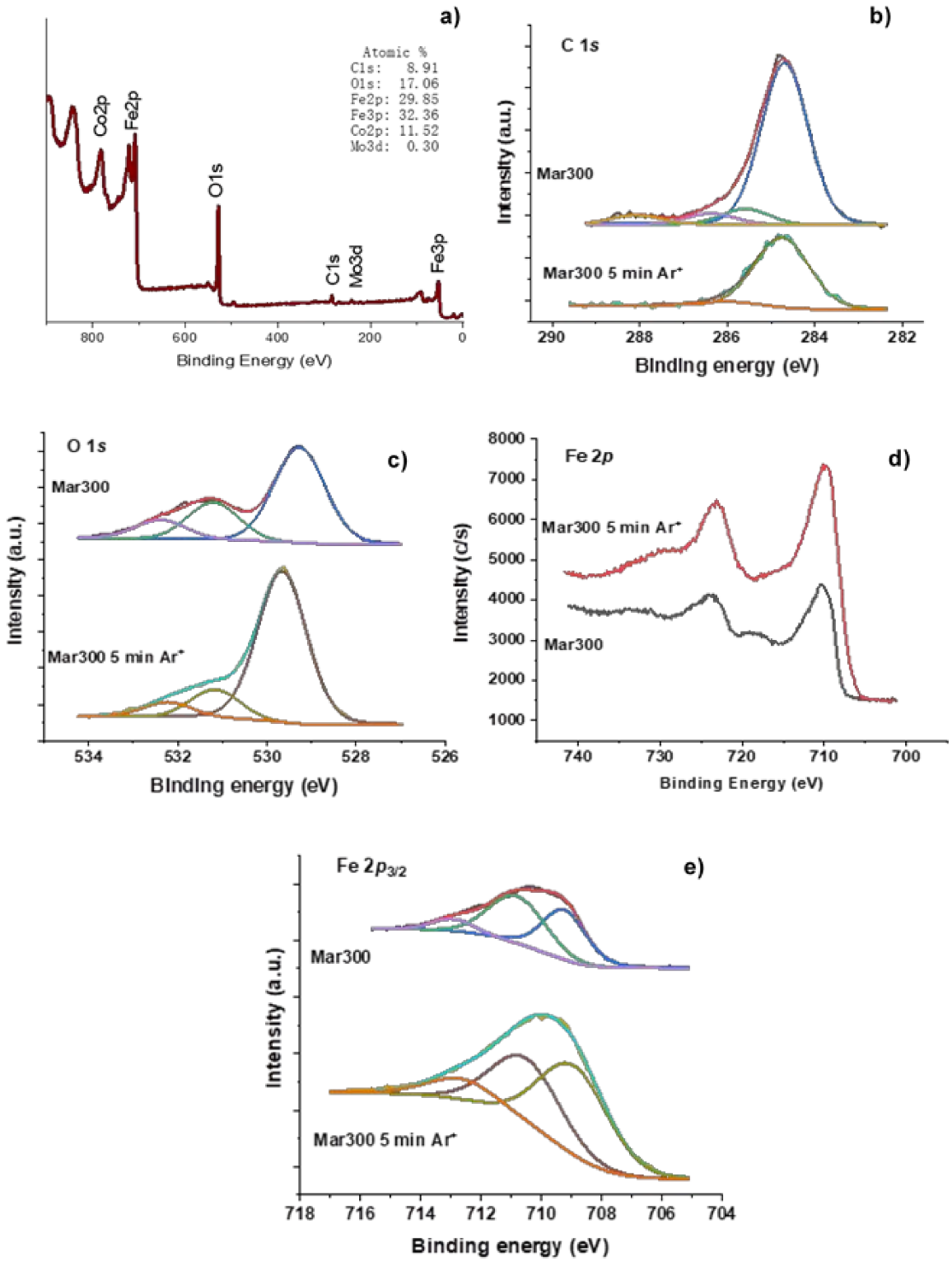

Figure 14. X-ray photoelectron spectroscopy (XPS) spectra of samples with the oxide produced on maraging steel 300 (Mar300) before and after etching for 5 min with Ar^+ plasma (Mar300 5 min Ar^+). (**a**) Survey spectrum of sample Mar300: (**b**) C 1*s*, (**c**) O 1*s*, (**d**) Fe 2*p*, and (**e**) Fe $2p_{3/2}$ deconvoluted.

Table 7. Surface chemical composition (in at. %) for the studied oxide produced on maraging steels before and after etching for 5 min with Ar^+ plasma.

Sample	C	O	Fe	Co	Mo
Mar300	47.94	38.57	10.13	3.24	0.12
Mar300 5 min Ar^+	18.41	42.35	31.12	8.14	0.00
Mar350	37.49	42.58	14.83	4.90	0.20
Mar350 5 min Ar+	10.82	41.60	36.64	18.19	0.38

The Fe 2*p* core-level spectra of the oxide produced on maraging steel 300 grade before and after etching for 5 min with Ar^+ are shown in Figure 14, where the deconvolution of the Fe $2p_{3/2}$ signal is also included, and the corresponding values of the different contributions are shown in Table 6. It is well known that the position of the contributions of the Fe $2p_{3/2}$ signal, as well as its satellite peak, are very sensitive to the oxidation state of iron [39–41]. It is clear that the etching process modified the Fe 2*p* signal. Upon etching, the intensity of the signal increased and the surface iron content increased from 10.13% to 31.12% in atomic concentration % (see Table 7). The deconvolution of the Fe $2p_{3/2}$ main peak of the samples is also shown in Figure 14e. This peak was deconvoluted in three contributions at 708.9–709.2 eV assigned to Fe^{2+}, 710.6–710.8 eV assigned to Fe^{3+}, and 712.6–712.9 eV related to an interaction of Fe^{2+} and Fe^{3+} [42]. It is interesting to know that the $Fe^{2+}/(Fe^{2+} + Fe^{3+})$ ratios on the surface of both samples were calculated from the XPS deconvolution (see Table 6), and as expected, the $Fe^{2+}/(Fe^{2+} + Fe^{3+})$ ratio increased after etching, indicating a higher proportion of the spinel phase $CoFe_2O_4$ and hematite [35,43–49]. This was also supported by the higher cobalt content after etching (Table 7) from 3.24% to 8.14% in at. %. The shape of the Fe 2*p* spectra also indicated that magnetite (Fe_3O_4) was not formed.

The Co 2*p* core-level spectra (not shown) were very complex. The Co 2*p* spectrum before etching showed a maximum at 781.3 eV assigned to Co^{2+}, but this assignation was complex because the presence of Co^{3+} species cannot be ruled out. Upon etching, two maxima were observed at 780.7 and 782.0 eV. The new contribution at low-binding energy was assigned to reduced Co species [47–52]. The Mo 3*d* signal was very noisy and hardly visible, and the Mo $3d_{5/2}$ presented a maximum at 232.1 eV, assigned to Mo^{6+} from MoO_3 [17,53,54]. Upon etching, the Mo 3d signal was not visible.

Figure 15 shows the survey spectra for the oxide produced on Mar350 maraging steel and the C 1*s*, O 1*s*, Fe 2*p*, and Mo 3*d* core-level spectra before and after etching for 5 min with Ar^+ plasma, and Tables 6 and 7 include the binding energy values (in eV) of the studied signals and the surface chemical compositions for the same samples. The C 1*s* high-resolution spectra (Figure 15b) were similar to those observed in the case of the maraging steel 300 grade sample, but the surface contents of C were lower, being 37.39% and 10.88% for the sample before and after etching. As aforementioned, some of the contributions of oxygen were due to the hydroxyl and hydrocarbon groups; the decrease of the carbon amount after etching was indicative of the fact that the surface of the oxide was less hydrophobic [35–38]. The O 1*s* core-level spectra also showed three contributions (Figure 15c and Table 6) at 529.7, 531.2, and 532. 4 eV, but in this case, the relative intensity of the surface lattice oxygen (O^{2-}) was much higher, and the surface content of O 1*s* was also higher compared to that observed for sample maraging steel 300 grade. This also points out the higher observed hydrophilicity. After etching, the surface content of oxygen was barely modified. The Fe 2*p* core-level spectrum for maraging steel 350 was different (Figure 15d,e), with a much lower relative intensity of the contribution at 708.5 eV assigned to Fe^{2+}, and the calculated $Fe^{2+}/(Fe^{2+} + Fe^{3+})$ ratio was much lower (0.17). This fact points out that, before etching, this sample presented a high concentration of cobalt spinel. After etching, the $Fe^{2+}/(Fe^{2+} + Fe^{3+})$ ratio increased to 40, but interestingly, the Fe/Co atomic ratio was 36.64/18.14 = 2.01, very near to the theoretical value for the cobalt spinel $CoFe_2O_4$. However, this was not compatible with the relative high content of Fe^{2+}.

The Co 2*p* spectrum (not shown) before etching showed two maxima at 780.7 and 782.7 eV, with a difficult assignation, but indicated the presence of Co^{2+} and Co^{3+}, although this assignation was complex. The possible formation of a surface cobalt spinel Co_3O_4 cannot be discarded together with the presence of the spinel $CoFe_2O_4$. Upon etching, one maximum was observed at 782.3 eV. The Mo 3*d* signal was then clearly observed (see Figure 15f), and the Mo $3d_{5/2}$ presented a maximum at 232.1 eV, assigned to Mo^{6+} from MoO_3 [17,53,54]. Before etching, the Mo 3*d* signal was modified with the appearance of a reduced oxide with a binding energy value of 229.6 eV, assigned to Mo^{4+} of MoO_2. In this case, after etching, the surface atomic concentration of Mo increased from 0.20% to 0.38%.

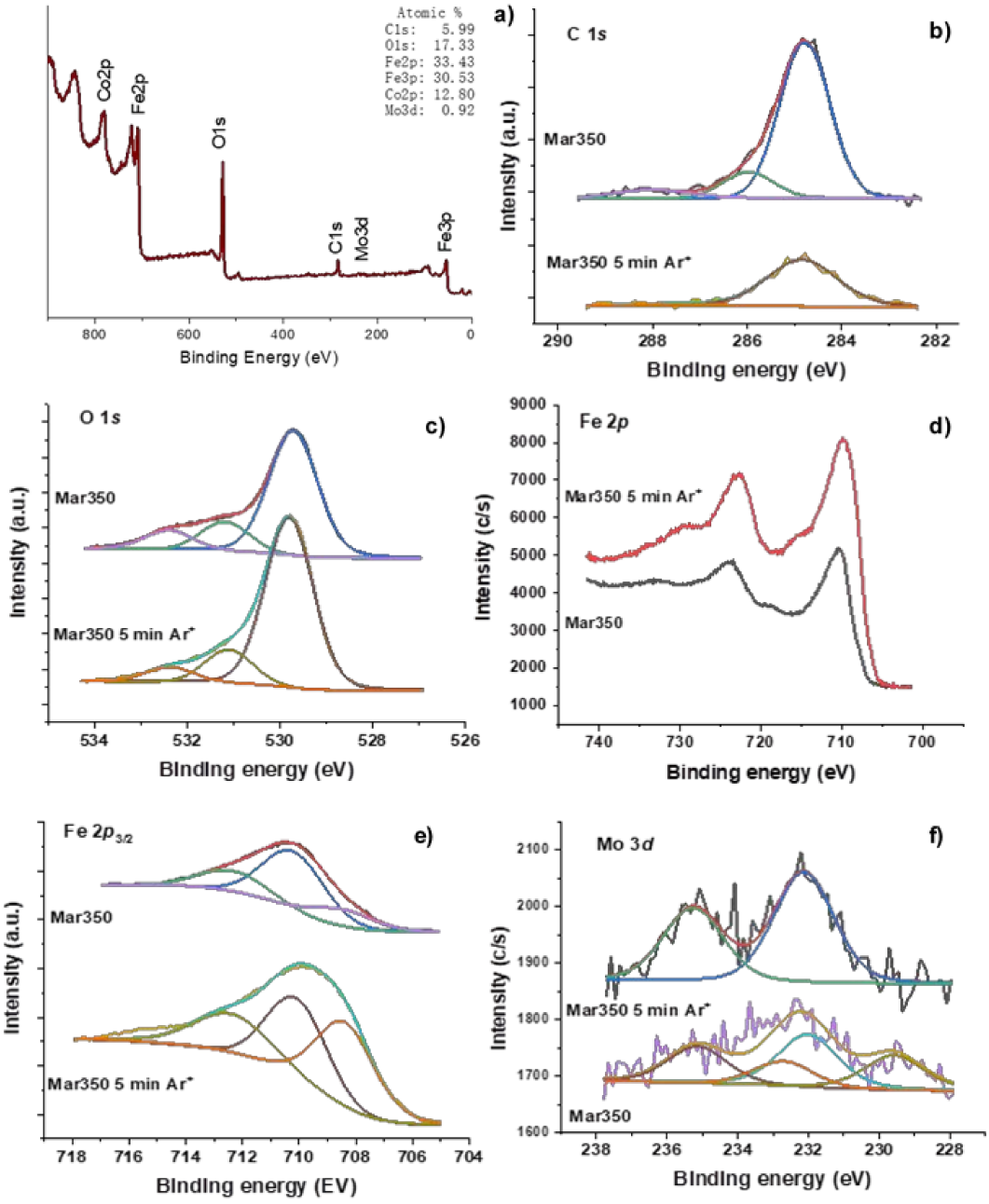

Figure 15. X-ray photoelectron spectroscopy (XPS) spectra of samples with the oxide produced on grade 350 maraging steel before (Mar350) and after etching for 5 min with Ar^+ plasma (Mar350 5 min Ar^+). (**a**) Survey spectrum of sample, (**b**) C 1*s*, (**c**) O 1*s*, (**d**) Fe 2*p*, (**e**) Fe $2p_{3/2}$ deconvoluted, and (**f**) Mo 3*d*.

3.3. Sliding Properties

Scratch tests led us to determine the adhesive damage between the oxide layer and the metallic maraging alloy substrate, also denoted as Pc2. Figure 16 (left hand side) exhibits the whole scratch track. The behavior was clearly discerned by comparing the micro-fracture events and damage features in regions close to the track edges. Figure 16 (right hand side) shows top-view field emission scanning electron microscopy (FE-SEM) images of nanoscratch tracks, where some interesting features are clearly visible—mainly, chipping, also known as decohesion. Furthermore, the Pc2 directly determined from the FE-SEM micrographs are summarized in Table 8. From Figure 16 and the data summarized in Table 8, it is clearly visible that the oxide layers grown on the maraging 350 alloy required a higher force in order to detach the oxide layer growth under the CO_2 atmosphere from the metallic maraging substrate.

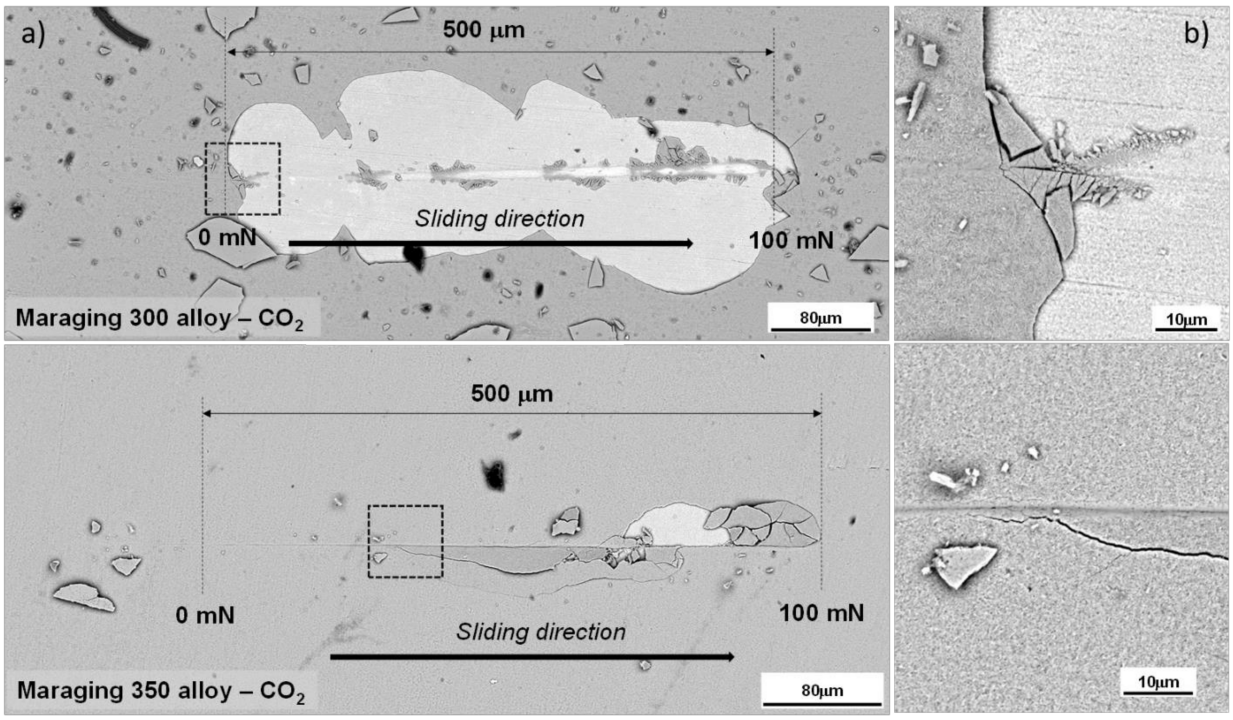

Figure 16. (**a**) Field emission scanning electron microscopy (FE-SEM) image for the nanoscratch track and (**b**) magnification of the top-view FE-SEM images of nanoscratch tracks where the first adhesive damage appears.

Table 8. Pc2 directly determined from the field emission scanning electron microscopy (FE-SEM) micrographs for each oxide produced on each maraging steel.

Maraging Steel	Pc2 (mN)
Mar300	2
Mar350	25

4. Discussion

The results on both oxide layers showed that the film was not homogeneous and that several phases formed the layer. The processes of how they are formed and grown have been approached by several authors from different points of view, and divergent information has been found. On the basis of the results found in this work, several points can be highlighted; one of them is that TiO_2 is in the innermost layers of the oxide, because it was not detected by X-ray photoelectron spectroscopy (XPS). Only the X-ray diffraction (XRD) that penetrated through different layers was able to detect it. This observation is

in fair agreement with References [55–57] and Klein et al. [1–3], based on thermodynamic information from experiments conducted under a steam atmosphere, which highlighted that, in the first stage of oxidation process, all elements were oxidized, and mainly titanium, which exhibited high reactivity with oxygen, but it ended up being covered by iron oxides because of the faster kinetics of the oxide formation reactions of this element. The same statement was made for MoO_3, but the results obtained from Raman and Fourier transform infrared (FT-IR) techniques detected this oxide in the outermost layers. These results were related to the chemical composition of steels, although the amount of molybdenum was similar between them, there was a difference in the amount of cobalt, which for this research was between 9.5 wt. % and 11.6 wt. %, which is slightly higher than the levels reported by Klein et al. [1–3], who reported a value of around 8 wt. %.

Klein et al. [1–3] and Rezek et al. [4] reported that the oxide formed was magnetite (Fe_3O_4), but in this research, cobalt ferrite, $CoFe_2O_4$, and hematite (α-Fe_2O_3) were found. According to the literature [16,58–62], also it is possible to generate hematite, and the main reaction to generate it is a diffusion reaction, specifically by the diffusion of cobalt and nickel in the form of Co^{2+} and Ni^{2+} species from the metallic matrix to the outside. These ions end up occupying the octahedral sites of spinel, replacing Fe^{2+} iron, and displacing it to the outside of the film, where it is exposed to a higher concentration of oxygen, and they are oxidized to Fe^{3+}. The formation of nickel-rich austenite in the oxide–metal interface is due to the decomposition of the martensite at temperatures above 500 °C [63]. However, remnants of iron and nickel may be subsequently present within the formed spinel [5,56,61,64,65]. This statement was confirmed with the results of the energy dispersive X-ray (EDS) measurements made on the surface of the oxide layer, where small amounts of nickel were detected.

The formation of hematite is related to the atmospheres used in the heat treatment in this research. Hong et al. [44] and Zhang et al. [66] described that iron-based materials oxidized at temperatures between 377 °C and 527 °C under steam, and mainly with CO_2 atmospheres, producing negative free energy for the formation of hematite; therefore, under these conditions, part of the magnetite exposed to higher concentrations of oxygen (outermost layers) is oxidized to hematite ($Fe_3O_4 \rightarrow \alpha$-$Fe_2O_3$) [56,62,66]. Genuzio et al. [62] also mentioned that the kinetics of this transformation are very fast and that it depends on the chemical composition and the availability of defects in the crystalline network, which allow for the growth of the new phase through specific crystallographic plans. According to Genuzio et al. [67], from 397 °C, α-Fe_2O_3 is formed in the middle of the magnetite, which grows dendritically and with morphological differences that distinguish it from the matrix. Similar differences were mentioned by Genuzio et al. [62], and these findings coincided with the protuberances found in the oxides of this research.

5. Conclusions

Both maraging steel grades studied in this research presented a non-homogeneous oxide layer, with several defects spread over the entire surface, such as holes that exposed more internal layers, cracks, porosity, and high roughness. The oxide formed was composed of four different phases, the majority being cobalt spinel ferrite ($CoFe_2O_4$), hematite (α-Fe_2O_3), molybdenum oxide (MoO_3), and titanium oxide (TiO_2).

The conditions of time, temperature, and atmospheres used in the heat treatment allowed us to have a percentage of more than 65% of spinel for both steels.

It was found that the chemical composition of the oxide changed over depth; the inner parts were richer in alloy elements, and in general, the outer ones were richer in iron. An example of this is that the largest amount of titanium, nickel, and molybdenum was found in the inner parts of the oxide. These findings were confirmed when TiO_2 and nickel-rich austenite were only detected by low-angle X-ray diffraction (XRD), which highlighted that these elements were located on the metal–oxide layer interface. This fact is related to a greater amount of cobalt in its chemical composition. This element acts so that

molybdenum forms fine intermetallic precipitates during aging, which ends up making it available on the surface and creates conditions for its oxidation.

The formation of hematite depended strongly on the temperatures, partial pressure of oxygen, and the atmospheres used in the heat treatments. Under these conditions, part of the surface magnetite turned into α-Fe_2O_3 with a different morphology and with a chemical composition with few alloying elements. The low diffusion of nickel, a product of the formation of rich austenite, in this element together with an increase in the chemical composition of cobalt in these steels (with its ions with a high preference for occupying the octahedral sites in the network) influenced the transformation of the initially formed magnetite in $CoFe_2O_4$ cobalt ferrite. However, different nickel contents were detected in energy dispersive X-ray (EDS) measurements made on the different exposed oxide layers, which means that, together with iron, this element can replace cobalt inside the spinel.

The maraging 350 steel presented a good adherence between the oxide layer and the metallic substrate growth under the CO_2 atmosphere. This demonstrates its capability for being used under aggressive conditions.

Author Contributions: Conceptualization, M.A.C.F., G.F.R. and M.J.G.d.S.; Data curation, M.A.C.F.; Formal Analysis, M.A.C.F., J.J.R.R., E.V.-G. and E.R.-C.; Funding acquisition, M.A.C.F., G.F.R., J.J.R.R., E.R.-C. and M.J.G.d.S.; Investigation, M.A.C.F., J.J.R.R., A.B.F.S. and E.R.-C.; Methodology, M.A.C.F., G.F.R. and M.J.G.d.S.; Project administration, M.A.C.F., G.F.R. and M.J.G.d.S.; Resources, J.J.R.R., E.V.-G., A.B.F.S., E.R.-C., G.F.R. and M.J.G.d.S.; Supervision, M.A.C.F., G.F.R. and M.J.G.d.S.; Validation, J.J.R.R., J.L.C., E.R.-C., G.F.R. and M.J.G.d.S.; Visualization, M.A.C.F., J.J.R.R., J.L.C., E.R.-C., G.F.R. and M.J.G.d.S.; writing—original draft preparation, M.A.C.F., J.J.R.R., J.L.C., E.V.-G. and E.R.-C.; writing—review and editing, M.A.C.F., J.J.R.R., J.L.C., E.R.-C., G.F.R. and M.J.G.d.S.; All authors have read and agreed to the published version of the manuscript.

Funding: This research received no external funding.

Institutional Review Board Statement: Not applicable.

Informed Consent Statement: Not applicable.

Data Availability Statement: Not applicable.

Acknowledgments: The authors gratefully acknowledge the CAPES/PRINT-UFC, FUNCAP and CNPq for financial assistance. The authors would like to thank the Central Analítica-UFC/CT-INFRA/MCTI-SISANO/Pró-Equipamentos CAPES, the Barcelona Research Center in Multiscale Science and Engineering—UPC, CIEFMA-UPC, LACAM-UFC, GPSA-UFC and NIM-UMA Research Groups for technical support. ERC thanks to projects RTI2018-099668-BC22 of Ministerio de Ciencia, Innovación y Universidades, and project UMA18-FEDERJA-126 of Junta de Andalucía and FEDER funds. Finally, J.J. Roa acknowledges the Serra Hunter programme of the "Generalitat de Catalunya".

Conflicts of Interest: The authors declare no conflict of interest.

References

1. Klein, I.; Sharon, J.; Yaniv, A. A mechanism of oxidation of ferrous alloys by super-heat steam. *Scr. Metall.* **1981**, *15*, 141–144. [CrossRef]
2. Klein, I.; Yaniv, A.; Sharon, J. The oxidation mechanism of Fe-Ni-Co alloys. *Oxid. Met.* **1981**, *16*, 1–2. [CrossRef]
3. Klein, I.; Yaniv, A.; Sharon, J. The mechanism of oxidation of Fe-Ni-Co alloys; The role of Ti And Mo. *Appl. Surf. Sci.* **1983**, *14*, 351–358. [CrossRef]
4. Rezek, J.; Klein, I.; Yahalom, J. Structure and corrosion resistance of oxides grown on maraging steel in steam at elevated temperatures. *Appl. Surf. Sci.* **1997**, *108*, 159–165. [CrossRef]
5. Greyling, C.; Kotzi, A.; Viljoen, P. The kinetics of oxide film growth on maraging steel as described by space-charge effects. *Surf. Interface Anal.* **1990**, *16*, 293–298. [CrossRef]
6. Chung, F. Quantitative interpretation of X-ray diffraction patterns of mixtures. I. Matrix-Flushing method for quantitative multicomponent analysis. *J. Appl. Cryst.* **1974**, *7*, 519. [CrossRef]
7. Zhou, X.; Liu, D.; Bu, H.; Deng, L.; Liu, H.; Yuan, P.; Du, P.; Song, H. XRD-based quantitative analysis of clay minerals using reference intensity ratios, mineral intensity factors, Rietveld, and full pattern summation methods: A critical review. *Solid Earth Sci.* **2018**, *3*, 16–29. [CrossRef]

8. Flamant, Q.; García, F.M.; Roa, J.J.; Anglada, M. Hydrofluoric acid etching of dental zirconia. Part 1: Etching mechanism and surface characterization. *J. Eur. Ceram. Soc.* **2016**, *36*, 121–134. [CrossRef]
9. Dong, W.P.; Sullivan, P.J.; Stout, K.J. Comprehensive study of parameters for characterising three-dimensional surface topography: III: Parameters for characterising amplitude and some functional properties. *Wear* **1994**, *178*, 29–43. [CrossRef]
10. Dong, W.P.; Sullivan, P.J.; Stout, K.J. Comprehensive study of parameters for characterising three-dimensional surface topography: IV: Parameters for characterising spatial and hybrid properties. *Wear* **1994**, *178*, 45–60. [CrossRef]
11. Viana, N.F.; Dos Santos, N.C.; De Abreu, H.F.G. The variant selection in the transformation from austenite to martensite in samples of maraging-350 steel. *J. Mater. Res. Technol.* **2013**, *2*, 298–302. [CrossRef]
12. Conde, F.F.; Escobar, J.D.; Oliveira, J.P.; Béreš, M.; Jardini, A.L.; Bose, W.W.; Avila, J.A. Effect of thermal cycling and aging stages on the microstructure and bending strength of a selective laser melted 300-grade maraging steel. *Mater. Sci. Eng. A* **2019**, *758*, 192–201. [CrossRef]
13. Capurro, C.; Cicutti, C. Analysis of titanium nitrides precipitated during medium carbon steels solidification. *J. Mater. Res. Technol.* **2018**, *7*, 342–349. [CrossRef]
14. Silva, C.; Farias, J.; Miranda, H.; Guimarães, R.; Menezes, J.A.M.; Neto, M. Microstructural characterization of the HAZ in AISI 444 ferritic stainless steel welds. *Mater. Charact.* **2008**, *59*, 528–533. [CrossRef]
15. JCPDS. *X-Ray Diffraction Data Cards of the Joint Committee on Powder Diffraction Standards*; International Center for Diffraction Data: Swarthmore, PA, USA, 1975.
16. Dąbrowa, J.; Stygar, M.; Mikuła, A.; Knapik, A.; Mroczka, K.; Tejchman, W.; Martin, M. Synthesis and microstructure of the $(Co,Cr,Fe,Mn,Ni)_3O_4$ high entropy oxide characterized by spinel structure. *Mater. Lett.* **2018**, *216*, 32–36. [CrossRef]
17. Zhao, N.; Fan, H.; Zhang, M.; Ma, J.; Du, Z.; Yan, B.; Li, H.; Jiang, X. Simple electrodeposition of MoO_3 film on carbon cloth for high-performance aqueous symmetric supercapacitors. *Chem. Eng. J.* **2020**, *390*, 124477. [CrossRef]
18. Magnée, A.; Drapier, J.M.; Dumont, J.; Coutsouradis, D.; Habraken, L. *Cobalt Containing High Strength Steels*; Centre d'Information du Cobalt: Brussels, Belgium, 1974; p. 128. Available online: http://refhub.elsevier.com/S0360-3199(19)31930-5/sref1 (accessed on 10 March 2020).
19. Vasudevan, V.; Kim, S.; Wayman, C. Precipitation reactions and strengthening behavior in 18 Wt Pct nickel maraging steels. *Metall. Trans. A* **1990**, *21*, 2655–2668. [CrossRef]
20. Sha, W.; Cerezo, A.; Smith, G.D.W. Phase chemistry and precipitation reactions in maraging steels: Part 4. Discussion and conclusion. *Metall. Trans. A* **1993**, *24*, 1251–1256. [CrossRef]
21. Lima Filho, V.; Barrosa, I.; Abreu, H. Influence of solution annealing on microstructure and mechanical properties of maraging 300 steel. *Mater. Res.* **2017**, *20*, 10–14. [CrossRef]
22. Ding, M.; Chen, W.; Xu, H.; Shen, Z.; Lin, T.; Hu, K.; Hui Lu, C.; Xie, Z. Novel α-Fe_2O_3/MXene nanocomposite as heterogeneous activator of peroxymonosulfate for the degradation of salicylic acid. *J. Hazard. Mater.* **2020**, *382*, 121064. [CrossRef]
23. Wang, Y.; Zhang, A.; Zhang, D.; Yang, J.; Li, H.; Meng, F.; Sun, Z.; Chen, G. Ultra-low loading of Ag_2CrO_4 on BiOI/$CoFe_2O_4$ microsphere with p-n heterojunction: Highly improved photocatalytic performance for Hg0 removal and mechanism insight. *J. Photochem. Photobiol. A Chem.* **2020**, *396*, 112543. [CrossRef]
24. Routray, K.L.; Saha, S.; Behera, D. Nanosized $CoFe_2O_4$-graphene nanoplatelets with massive dielectric enhancement for high frequency device application. *Mater. Sci. Eng. B* **2020**, *257*, 114548. [CrossRef]
25. Li, Y.; Wang, Y.; Lu, H.; Li, X. Preparation of $CoFe_2O_4$eP4VP@Ag NPs as effective and recyclable catalysts for the degradation of organic pollutants with NaBH4 in water. *Int. J. Hydrog. Energy* **2020**, *45*, 16080–16093. [CrossRef]
26. Yang, Z.; Li, Y.; Xhang, X.; Cui, X.; He, S.; Liang, H.; Ding, A. Sludge activated carbon-based $CoFe_2O_4$-SAC nanocomposites used as heterogeneous catalysts for degrading antibiotic norfloxacin through activating peroxymonosulfate. *Chem. Eng. J.* **2020**, *384*, 123319. [CrossRef]
27. Sharma, P.K.; Raghubanshi, A.S.; Shah, K. Examining dye degradation and antibacterial properties of organically induced α-MoO_3 nanoparticles, their uptake and phytotoxicity in rice seedlings. *Environ. Nanotechnol. Monit. Manag.* **2020**, *14*, 100315. [CrossRef]
28. Ramar, V.; Balasubramanian, K. Optical and highly enhanced solar light-driven photocatalytic activity of reduced graphene oxide wrapped α-MoO_3 nanoplates. *Sol. Energy* **2019**, *194*, 1–10. [CrossRef]
29. Guo, R.; Dang, L.; Liu, Z.; Lei, Z. Incorporation of electroactive $NiCo_2S_4$ and Fe_2O_3 into graphene aerogel for high-energy asymmetric supercapacitor. *Colloids Surf. A* **2020**, *602*, 125110. [CrossRef]
30. De Faria, D.L.A.; Lopes, F.N. Heated goethite and natural hematite: Can Raman spectroscopy be used to differentiate them? *Vib. Spectrosc.* **2007**, *45*, 117–121. [CrossRef]
31. Wang, W.; Ding, Z.; Zhao, X.; Wu, S.; Li, F.; Yue, M.; Liu, J.P. Microstructure and magnetic properties of MFe_2O_4 (M = Co, Ni, and Mn) ferrite nanocrystals prepared using colloid mill and hydrothermal method. *J. Appl. Phys.* **2015**, *117*, 17A328. [CrossRef]
32. De La Figuera, J.; Quesada, A.; Martín-García, L.; Sanz, M.; Oujja, M.; Rebollar, E.; Castillejo, M.; Prieto, P.; Muñoz-Martín, A.; Aballe, L.; et al. Self-organized single crystal mixed magnetite/cobalt ferrite films grown by infrared pulsed-laser deposition. *Appl. Surf. Sci.* **2015**, *359*, 480–485. [CrossRef]
33. Yang, J.; Xiao, X.; Chen, P.; Zhu, K.; Cheng, K.; Ye, K.; Wang, G.; Cao, D.; Yan, J. Creating oxygen-vacancies in MoO_3-x nanobelts toward high volumetric energy-density asymmetric supercapacitors with long lifespan. *Nano Energy* **2019**, *58*, 455–465. [CrossRef]

34. Reed, B.W.; Williams, D.R.; Moser, B.P.; Koski, K.J. Chemically tuning quantized acoustic phonons in 2D layered MoO_3 nanoribbons. *Nano Lett.* **2019**, *19*, 4406–4412. [CrossRef] [PubMed]
35. Kaspar, P.; Sobola, D.; Dallaev, R.; Ramazanov, S.; Nebojsa, A.; Rezaee, S.; Grmela, L. Characterization of Fe_2O_3 thin film on highly oriented pyrolytic graphite by AFM, Ellipsometry and XPS. *Appl. Surf. Sci.* **2019**, *493*, 673–678. [CrossRef]
36. Barreca, D.; Battiston, G.A.; Berto, D.; Gerbasi, R.; Tondello, E. Chemical vapor deposited Fe_2O_3 thin films analyzed by XPS. *Surf. Sci. Spectra* **2001**, *8*, 240. [CrossRef]
37. Galtayries, A.; Sporken, R.; Riga, J.; Blanchard, G.; Caudano, R. XPS comparative study of ceria/zirconia mixed oxides: Powders and thin film characterization. *J. Electron Spectrosc.* **1998**, *88*, 951–956. [CrossRef]
38. Barr, T.L. An ESCA study of the termination of the passivation of elemental metals. *J. Phys. Chem.* **1978**, *82*, 1801–1810. [CrossRef]
39. Grosvenor, A.P.; Kobe, B.A.; Biesinger, M.C.; Mcintyre, N.S. Investigation of multiplet splitting of Fe 2*p* XPS spectra and bonding in iron compounds. *Surf. Interface Anal.* **2004**, *36*, 1564–1574. [CrossRef]
40. Lin, T.C.; Seshadri, G.; Kelber, J.A. A consistent method for quantitative XPS peak analysis of thin oxide films on clean polycrystalline iron surfaces. *Appl. Surf. Sci.* **1997**, *119*, 83–92. [CrossRef]
41. Sanchis, R.; Alonso-Domínguez, D.; Dejoz, A.; Picom, M.P.; Álvarez-Serrano, I.; García, T.; López, M.L.; Solsona, B. Eco-friendly cavity-containing iron oxides prepared by mild routes as very efficient catalysts for the total oxidation of VOCs. *Materials* **2018**, *11*, 1387. [CrossRef]
42. Lu, L.; Ai, Z.; Li, J.; Zheng, Z.; Li, Q.; Zhang, L. Synthesis and characterization of Fe–Fe_2O_3 core–shell nanowires and nanoneckaces. *Cryst. Growth Des.* **2007**, *7*, 459–464. [CrossRef]
43. Yi, Y.; Wu, Q.; Wang, W.; Cui, C. In situ depositing an ultrathin CoOxHy layer on hematite in alkaline media for photoelectrochemical water oxidation. *Appl. Catal. B Environ.* **2020**, *263*, 118334. [CrossRef]
44. Hong, H.; Memon, N.K.; Dong, Z.; Kear, B.H.; Tse, S.D. Flame synthesis of gamma-iron-oxide (γ-Fe_2O_3) nanocrystal films and carbon nanotubes on stainless-steel substrates. *Proc. Combust. Inst.* **2019**, *37*, 1249–1256. [CrossRef]
45. Hu, X.; Yu, J.C.; Gong, J.; Li, Q.; Li, G. α-Fe_2O_3 Nanorings Prepared by a Microwave-Assisted Hydrothermal Process and Their Sensing Properties. *Adv. Mater.* **2007**, *19*, 2324–2329. [CrossRef]
46. Liu, W.; Cheng, B.; Miao, T.; Xie, J.; Liu, L.; Si, J.; Zhou, G.; Qin, H.; Hu, J. Room temperature electric field control of magnetic properties for the α-Fe_2O_3/Fe_3O_4 composite structure. *J. Magn. Magn. Mater.* **2019**, *491*, 165500. [CrossRef]
47. Zhang, T.; Li, Z.; Wang, L.; Zhang, Z.; Wang, S. Spinel $CoFe_2O_4$ supported by three dimensional graphene as high-performance bi-functional electrocatalysts for oxygen reduction and evolution reaction. *Int. J. Hydrog. Energy* **2019**, *44*, 1610–1619. [CrossRef]
48. Yan, W.; Cao, X.; Tian, J.; Jin, C.; Ke, K.; Yang, R. Nitrogen/sulfur dual-doped 3D reduced graphene oxide networks-supported $CoFe_2O_4$ with enhanced electrocatalytic activities for oxygen reduction and evolution reactions. *Carbon* **2016**, *99*, 195–202. [CrossRef]
49. Yan, W.; Bian, W.; Jin, C.; Tian, J.H.; Yang, R. An Efficient Bi-functional electrocatalyst based on strongly coupled $CoFe_2O_4$/Carbon nanotubes hybrid for Oxygen reduction and Oxygen evolution. *Electrochim. Acta* **2015**, *177*, 65–72. [CrossRef]
50. Zhao, Y.; Nie, G.; Ma, X.; Xu, P.; Zhao, X. Peroxymonosulfate catalyzed by rGO assisted $CoFe_2O_4$ catalyst for removing Hg0 from flue gas in heterogeneous system. *Environ. Pollut.* **2019**, *249*, 868–877. [CrossRef]
51. Fantauzzi, M.; Secci, F.; Angotzi, M.S.; Passiu, C.; Cannas, C.; Rossi, A. Nanostructured spinel cobalt ferrites: Fe and Co chemical state, cation distribution and size effects by X-ray photoelectron spectroscopy. *RSC Adv.* **2019**, *9*, 19171–19179. [CrossRef]
52. Ji, G.B.; Tang, S.L.; Ren, S.K.; Zhang, F.M.; Gu, B.X.; Du, Y.W. Simplified synthesis of single-crystalline magnetic $CoFe_2O_4$ nanorods by a surfactant-assisted hydrothermal process. *J. Cryst. Growth* **2004**, *270*, 156–161. [CrossRef]
53. Srinivasan, P.; Ravappan, J.B.B. Growth of α-MoO_3 Golf Ball Architectures with Interlocking Loops for Selective Probing of Trimethylamine at Room Temperature. *Mater. Res. Bull.* **2020**, *130*, 110944. [CrossRef]
54. Rajagopal, S.; Nataraj, D.; Khyzhum, O.Y.; Djaoued, Y.; Robichaud, J.; Senthil, K.; Mangalaraj, D. Systematic synthesis and analysis of change in morphology, electronic structure and photoluminescence properties of pyrazine intercalated MoO_3 hybrid nanostructures. *CrystEngComm* **2011**, *13*, 2358–2368. [CrossRef]
55. Surman, P.L. The oxidation of iron at controlled Oxygen partial pressures—I. Hydrogen/Water vapour. *Corros. Sci.* **1973**, *13*, 113–124. [CrossRef]
56. Subbaraman, R.; Deshmukh, S.A.; Sankaranarayanan, S.K. Atomistic insights into early stage oxidation and nanoscale oxide growth on Fe (100), Fe (111) and Fe (110) surfaces. *J. Phys. Chem. C* **2013**, *117*, 5195–5207. [CrossRef]
57. Luo, D.W.; Shen, Z.S. Oxidation behavior of Kovar alloy in controlled atmosphere. *Acta Metall. Sin. Engl. Lett.* **2008**, *21*, 409–418. [CrossRef]
58. Tsukimura, K.; Sasaki, S.; Kimizuka, N. Cation distributions in Nickel ferrites. *Jpn. J. Appl. Phys.* **1997**, *36*, 3609. [CrossRef]
59. Rodrigues, A.P.G.; Gomes, D.K.S.; Araújo, J.H.; Melo, D.M.A.; Oliveira, N.A.S.; Braga, R.M. Nanoferrites of nickel doped with cobalt: Influence of Co^{2+} on the structural and magnetic properties. *J. Magn. Magn. Mater.* **2015**, *374*, 748–754. [CrossRef]
60. Bliem, R.; Pavelec, J.; Gamba, O.; Mcdermott, E.; Wang, Z.; Gerhold, S.; Wagner, M.; Osiecki, J.; Schulte, K.; Schmid, M.; et al. Adsorption and incorporation of transition metals at the magnetite Fe_3O_4 (001) surface. *Phys. Rev. B* **2015**, *92*, 75440. [CrossRef]
61. Pardavi-Horvath, M. Microwave applications of soft ferrites. *J. Magn. Magn. Mater.* **2000**, *215–216*, 171–183. [CrossRef]
62. Genuzio, F.; Sala, A.; Schmidt, T.; Menzel, D.; Freund, H.-J. Phase transformations in thin iron oxide films: Spectromicroscopic study of velocity and shape of the reaction fronts. *Surf. Sci.* **2016**, *648*, 177–187. [CrossRef]

63. Silva, M.J.G.; Cardoso, J.L.; Carvalho, D.S.; Santos, L.P.M.; Herculano, L.F.G.; Abreu, H.F.G.; Pardal, J.M. The effect of prior austenite grain size on hydrogen embrittlement of Co-containing 18Ni 300 maraging steel. *Int. J. Hydrog. Energy* **2019**, *44*, 18606–18615. [CrossRef]
64. Jeon, B.; Van Overmeere, Q.; Van Duin, A.C.; Ramanathan, S. Nanoscale oxidation and complex oxide growth on single crystal iron surfaces and external electric field effects. *Phys. Chem. Chem. Phys.* **2013**, *15*, 1821–1830. [CrossRef]
65. Parkinson, G.S. Iron oxide surfaces. *Surf. Sci. Rep.* **2016**, *71*, 272–365. [CrossRef]
66. Zhang, X.; Yang, S.; Yang, Z.; Xu, X. Kinetics and intermediate phases in epitaxial growth of Fe_3O_4 films from deposition and thermal reduction. *J. Appl. Phys.* **2016**, *120*, 085313. [CrossRef]
67. Genuzio, F.; Sala, A.; Schmidt, T.; Menzel, D.; Freund, H.-J. Interconversion of α-Fe_2O_3 and Fe_3O_4 thin films: Mechanisms, morphology, and evidence for unexpected substrate participation. *J. Phys. Chem. C* **2014**, *118*, 29068–29076. [CrossRef]